Ghost Polarization Communication

Markus Rosskopf, Till Mohr, and Wolfgang Elsäßer*
Institute of Applied Physics, Technische Universität Darmstadt, 64289 Darmstadt, Germany

(Received 18 September 2019; revised manuscript received 18 October 2019; accepted 28 February 2020; published 25 March 2020)

There is an increasing and demanding interest in the realization of secure communication schemes. Here, we conceive and realize an approach for a message-encoding scheme between two parties, Alice and Bob, by exploiting the infinite number of polarization states of unpolarized thermal light on the Poincaré sphere together with their correlation properties to camouflage and recover a message, thus realizing ghost polarization communication. At first, we investigate the second-order correlation coefficient $g^{(2)}(\tau)$ of classical unpolarized broadband amplified-spontaneous-emission light emitted by an erbium-doped fiber amplifier at 1550 nm by manipulating its instantaneous polarization state utilizing various polarization optics in the beam paths of a Hanbury-Brown and Twiss like ghost polarimetry setup using ultra-fast two-photon absorption in a photomultiplier tube. The observed polarization state modifications are in excellent agreement with our developed model based on the Stokes vector dynamics and a Glauber protocol for $g^{(2)}(\tau)$. On the basis of these results we then proceed towards the realization of a message-encoding scheme. By changing the instantaneous polarization state using a half-wave plate, Alice encodes and subsequently transmits a message. The camouflaged message can be recovered uniquely by Bob measuring the second-order correlations of the modified instantaneous polarization state with his reference beam. By using the agreed keypad of the communication scheme, he is able to retrieve the bit values of the encoded message. Finally, we address real-world implementation of this first proof-of-principle demonstration and discuss its security issues. This scheme demonstrates a method of establishing a secure communication link between two parties directly on the physical layer based on polarization correlations of classical light. It is expected that by the realization of this correlated photon modality not only avenues for ghost modalities, in general, are opened but also insight into polarization, even more than 175 years after Stokes will be achieved.

DOI: 10.1103/PhysRevApplied.13.034062

I. INTRODUCTION

Secure communication is currently an important and challenging topic [1] for global digital-data exchange and ensures the interaction of Internet-of-Things devices as well as the private messaging between two parties (commonly called Alice and Bob). A frequently deployed system is the Rivest-Shamir-Adleman (RSA) public key cryptosystem [2], which is commonly used to secure web servers, emails, and credit-card payment systems [3]. Many efforts have been made in breaking the RSA system [3], but the most critical security vulnerability would arise from an efficient factoring using Shor's algorithm [4] on a quantum computer [5]. With the efforts made in the development of quantum computers [6], secure cryptographic systems are of recent interest [7], and alternative communication schemes like quantum cryptography are developed [8]. The latter ensures security due to the no-cloning theorem of quantum mechanics [9], which forbids perfectly cloning a quantum state [10]. Two important protocols for quantum communication are the BB84 [8] and Ekert [11] protocol, which have been implemented for free-space [12–14], satellite-based [15], and fiber-based [16] communication.

Apart from quantum cryptography, chaos communication is another area of research that aims to realize the secure transfer of information on the basis of physical laws [17–19]. In simple bidirectional communication schemes two lasers operating in the chaotic regime are coupled and the synchronization between them allows for the extraction of the information that has been camouflaged in the chaotic emission, thus providing a measure of security directly on the physical layer of the Open Systems Interconnection (OSI) model [20,21]. More elaborate schemes have demonstrated high bit rates and transmission robustness in a real-world scenario using these lasers operating in chaotic mode [22–24].

Another approach [25,26] that is used to achieve optical encryption is based on a technique called ghost imaging. At first, the ghost imaging scheme was observed with

*elsaesser@physik.tu-darmstadt.de

entangled photons [27]. Later, it was found that ghost imaging can be performed by using a classical pseudothermal source or even with sunlight and that the underlying physics can be described comprehensively by classical coherence propagation [28–32]. This imaging scheme can be seen as one part of various ghost modalities, all relying on the correlation of photons. In this framework, experiments on ghost spectroscopy [33–35], temporal ghost imaging [36,37], and ghost polarimetry [38] have been demonstrated. In principle, the latter scheme would enable the transmission of a camouflaged message [38] by hiding and subsequently recovering a polarization state, comparable to the idea behind chaos communication [39].

Here, we pursue an approach for a secure message-encoding scheme based on polarization correlations of classical unpolarized light, such that the message can be camouflaged and subsequently retrieved in a way which has similarities to chaos cryptography concerning the idea of using the physical layer to encode and retrieve the message. However, here we now exploit the infinite number of polarization states on the Poincaré sphere as a basis for encoding. The polarization state of light can be described entirely by a four-valued Stokes vector [40], consisting of the intensity S_0 and three polarization components S_1, S_2, and S_3 representing a vector on the Poincaré sphere [41]. For completely unpolarized light, such as amplified spontaneous emission (ASE), e.g., emitted by an erbium-doped fiber amplifier (EDFA), the components S_1 to S_3 are zero. These components keep their zero value when the light passes through a wave plate, whose properties are described in terms of the Mueller matrix formalism. However, these values of the Stokes parameters are stationary values, which do not account for any ultra-fast polarization-state dynamics of unpolarized light. And, indeed, a novel dynamic description of unpolarized light was recently introduced [42]. Here, the polarization is described as an instantaneous polarization state (IPS), which can move randomly on the Poincaré sphere [42,43]. The time in which the IPS does not deviate significantly from its original state refers to the polarization time. This characteristic time is in the femtosecond regime and can be measured by detecting ultra-fast polarization correlations using two-photon absorption [44]. We directly use these ultra-fast polarization-state dynamics and investigate the influence of wave plates on the IPS of unpolarized light emitted by an EDFA. These IPS modifications are then used to conceive a proof-of-concept experiment for the secure data transfer between two parties, thus demonstrating its functionality in hiding and securely recovering a message.

II. EXPERIMENTAL SETUP

The idea behind the communication scheme is now realized within the frame of a Hanbury-Brown and Twiss ghost imaging or ghost polarimetry setup, which is schematically depicted in Fig. 1. Here we design our scheme in the sense that the reference beam [45] remains solely and securely on Bob's side and the object beam is directed to Alice, who encodes a message on it and redirects it back to Bob. He then recovers the message by exploiting the polarization correlation properties between his reference beam and the object beam that contains the message encoded by Alice. The unpolarized light emitted by the EDFA is divided equally into a reference and an object arm of roughly equal lengths by a nonpolarizing beam-splitter cube. The light source, beam splitter, delay stage, photomultiplier, quarter-wave plate (QWP $\lambda/4$), and a linear polarizer are located at Bob's part of the experiment, who wants to receive the message from Alice. After the IPS is modified by Bob's QWP, the light in the object arm is sent to Alice, who uses this part of the light to encode her message. She modifies the IPS using different half-wave plate (HWP, $\lambda/2$) orientations to encode her message. The light passes a fixed linear polarizer (LP_O) on Alice's side and finally is sent back to Bob where the two arms are combined again by a fiber coupler and the superimposed light is focused onto the cathode of a photomultiplier tube (PMT), which together with the variable delay stage (τ) enables the determination of the second-order correlation coefficient $g^{(2)}(\tau)$. All second-order correlation measurements for quantifying the polarization correlations and for extracting the message have been determined via interferometric autocorrelation functions recording the two-photon absorption counts of the PMT as a function of the realized displacement of the delay stage. Such a measured interferogram is shown on the bottom left side of Fig. 1. From this interferogram the normalized $g^{(2)}(\tau)$ coefficient is obtained by low-pass filtering [46] and a spline fit to the filtered curve is used to extract the value $g^{(2)}(\tau = 0)$. The resulting spline curve for the $g^{(2)}(\tau)$ coefficient is shown on the bottom right-hand side of Fig. 1. A value of $g^{(2)}(\tau = 0)$ of 2 is obtained for fully polarized thermal light (photon bunching), while a value of 1 indicates coherent light (no photon bunching). For the correlation coefficient of unpolarized thermal light without any polarization optics in the interferometer, a value of $g^{(2)}(\tau = 0) = 1.5$ is obtained [47]. Furthermore, the degree of polarization of the unpolarized thermal light of the EDFA used in this setup is measured to be 0.02 [38].

III. RESULTS

A. Experimental polarization correlation results

First, in preparation and as the basis for the communication scheme, the $g^{(2)}(0)$ values are measured as a function of the rotation angle between the two LPs without any wave plate in the object arm. The LP_R and LP_O are placed in the positions shown in Fig. 1. The results are depicted in Fig. 2 as solid black triangles. An angle of 0° corresponds to the LPs rotated parallel to each other. For this case, the

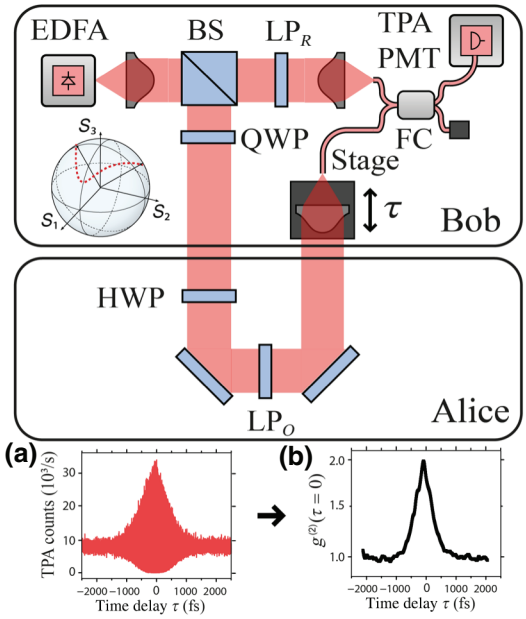

FIG. 1. Experimental setup enabling a secure message transfer from Alice to Bob by exploiting polarization correlations of photons. Top: Alice encodes her message as a rotation angle of the half-wave plate. The resulting IPS change can be measured by Bob using the two-photon absorption of a PMT (TPA PMT) and exploiting the polarization correlation between reference beam and object beam. Further components depicted are as follows: erbium-doped fibre amplifier, quarter-wave plate, beam-splitter cube (BS), linear polarizer (LP$_R$) in the reference arm, linear polarizer (LP$_O$) in the object arm and fiber coupler (FC). Below the EDFA, there is a schematic depiction of the Poincaré sphere, which is spanned up by the three Stokes parameters S_1, S_2, and S_3 and the temporal IPS dynamics on its surface is illustrated by the red-dot curve. Bottom: extraction of the $g^{(2)}(\tau)$ coefficient [right, (b)] from a measured fringe-resolved interferometric autocorrelation function [left, (a)].

light of the two interferometer arms is correlated since the $g^{(2)}(0)$ value is 2. By increasing the LP$_R$ rotation angle, the $g^{(2)}(0)$ values approach a value of 1 as the two LPs are orientated orthogonally to each other. These results confirm the Malus law for this ghost polarimetry setup [38]. In this setup, the $g^{(2)}$ values (solid black triangles) depicted in Fig. 2 are fitted by a function of the following form:

$$g^{(2)}(\tau = 0, \vartheta) = 1.5 + 0.5\cos(2\vartheta), \tag{1}$$

where ϑ is the LP$_R$ rotation angle with respect to the LP$_O$. This function is derived using a model that is discussed in the appendix of this paper. Using basic trigonometric identities, this formula can be rewritten in a form that is equivalent to the Malus law:

$$g^{(2)}(\tau = 0, \vartheta) = 1 + \cos^2(\vartheta). \tag{2}$$

We now place a HWP at a rotation angle of 45° in front of the fixed LP$_O$. As a result, the $g^{(2)}$ curve is shifted by

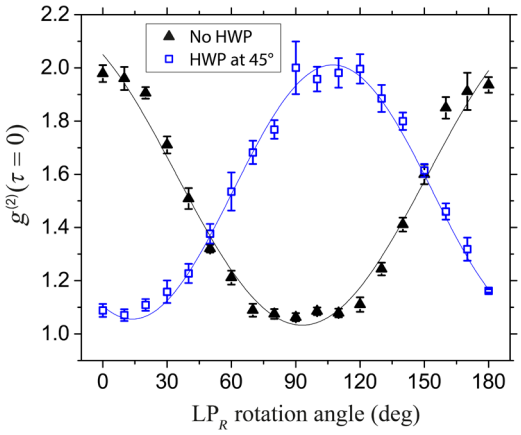

FIG. 2. Polarization correlations for LPs. Values of $g^{(2)}(\tau = 0)$ as a function of the rotation angle of the linear polarizer LP$_R$ in the reference arm for a fixed rotation angle of LP$_O$ (solid black triangles). Placing an additional half-wave plate oriented at 45° with respect to the fixed LP$_O$ and measuring the $g^{(2)}(\tau = 0)$ values yields the data points indicated by open blue squares. Continuous lines show the fits using Eqs. (1) and (3). The precision of the depicted $g^{(2)}(\tau = 0)$ measurement results is defined by the statistical error resulting from five subsequent measurements and is indicated in all experimental data sets by the error bars.

approximately 90° to the right (Fig. 2, blue squares), as the IPS is also rotated by 90° due to the influence of the HWP. Here, the $g^{(2)}$ values (open blue squares) depicted in Fig. 2 are fitted using the following function:

$$g^{(2)}(\tau = 0, \vartheta, \beta) = 1.5 + 0.5\cos[2(\vartheta - 2\beta)], \tag{3}$$

where ϑ is the LP$_R$ rotation angle and β is the HWP rotation angle. This function is also derived in the appendix.

After having successfully recovered the phase shift introduced by the HWP on the unpolarized light of the EDFA, in a second experiment the HWP is replaced by a QWP to generate elliptical and circular IPS, depending on the rotation angle of the QWP. The measured $g^{(2)}$ values for linear, elliptical, and circular polarization are shown in Fig. 3 as solid red circles, solid orange triangles, and open green diamonds, respectively.

In the case of a linear IPS with a QWP rotation angle of 0° the $g^{(2)}$ values are modulated between 1 and 2 for the various LP$_R$ rotation angles. For an LP$_R$ rotation angle of 0°, the polarizers LP$_R$ and LP$_O$ are aligned in parallel and a maximum $g^{(2)}$ value of 2 is obtained. Similar to the results obtained without any wave plate as depicted in Fig. 2, the $g^{(2)}$ values decrease, when the polarizers are aligned orthogonally to each other for a LP$_R$ rotation angle of 90°. However, for this setup, the $g^{(2)}$ values depicted in Fig. 3 are fitted by a function of the following form:

$$g^{(2)}(\tau = 0, \vartheta, \alpha) = 1.5 + 0.25\cos(2\vartheta) + 0.25\cos[2(\vartheta - 2\alpha)], \tag{4}$$

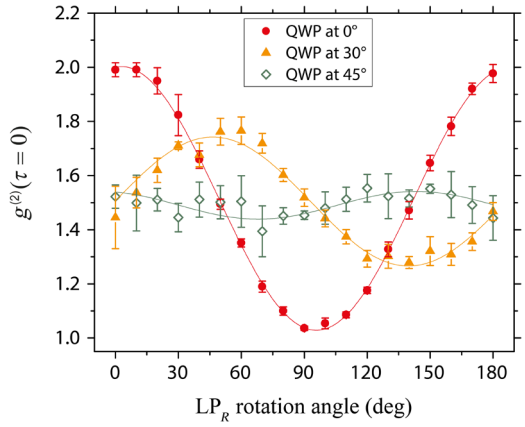

FIG. 3. Polarization correlations for LP and QWP. Values of $g^{(2)}(\tau = 0)$ as a function of the linear polarizer LP$_R$ rotation angle in the reference arm. The $g^{(2)}(\tau = 0)$ values for a quarter-wave plate rotation angle of 0° indicate an unpolarized IPS (solid red circles), whereas the $g^{(2)}(\tau = 0)$ values for rotation angles of 30° and 45° show an elliptical IPS (closed orange triangles) and a circular IPS (open green diamonds), respectively. The continuous lines are fitted to the data points using Eq. (4).

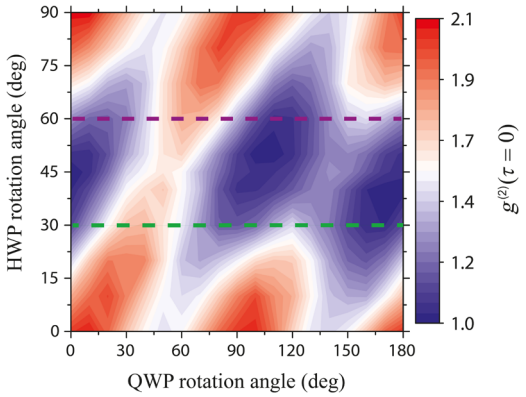

FIG. 4. Communication keypad. Values of $g^{(2)}(\tau = 0)$ measured by Bob as a function of the HWP (Alice) and QWP (Bob) rotation angle. The dashed lines indicate the two HWP angles used for encoding: 30° represent a "0" (green dashes) and 60° represent a "1" (purple dashes). The data points across the dashed lines are the data in Fig. 6.

where ϑ and α are the LP$_R$ and the QWP rotation angles, respectively. The origin of this function is also discussed in further detail in the appendix. When the rotation angle of the QWP is increased, the range of the $g^{(2)}$ values is reduced and the values are shifted to the right, when increasing the LP$_R$ rotation angles from 0° to 180°. This behavior can clearly be observed for the case of an elliptical IPS for a QWP rotation angle of 30° (solid orange triangles in Fig. 3). When the QWP is rotated to 45°, all of the $g^{(2)}$ values are nearly constant at 1.5 for all rotation angles of the LP$_R$, as can be seen in Fig. 3 (open green diamonds). This indicates that the IPS is transformed into a circular polarization state for all rotation angles of the LP$_R$. This demonstrates that by placing the QWP in front of the LP$_O$, we generate all possible elliptical IPS for unpolarized light that are represented by the respective $g^{(2)}(\tau = 0)$ values.

By using a combination of HWP, QWP, LP$_R$, and LP$_O$ placed at the respective positions depicted in Fig. 1, these results show that we can generate all possible polarization states on the Poincaré sphere [48].

The presented experimental results of the second-order correlation coefficient $g^{(2)}$ resemble the intensity measured for the corresponding polarization state after passing a linear polarizer in classical Stokes parameter analysis [48]. However, these characteristic curves of the intensity can only be achieved for completely polarized light as the Stokes vector of unpolarized light is given by $(1, 0, 0, 0)$ and thus does not change after passing a wave plate. In our experiments, we reveal an analogous behavior of the second-order correlation coefficient for the unpolarized light emitted by our EDFA in comparison to completely polarized light in a classical Stokes parameter analysis.

B. Communication scheme

In order to now realize a camouflaging communication scheme based on the polarization correlations and the shown IPS modifications, both the HWP and QWP are placed into the object arm as depicted in Fig. 1 and the influence of their rotation angle on the $g^{(2)}(\tau = 0)$ value measured by Bob is investigated. These angles are iterated from 0° to 90° and from 0° to 180° in 10° steps, respectively. Here, an angle of 0° corresponds to an optical axis orientation parallel to the LPs. The resulting two-dimensional map of $g^{(2)}(\tau = 0)$ values is shown in Fig. 4, where a value of 2 is represented by a red coloring and a value of 1 is given in the bluish areas of the figure.

Holding the HWP angle fixed at 0° and rotating the QWP angle the $g^{(2)}$ values alter between a maximum of 2 and 1.4 with a periodicity of 90°. Increasing the rotation angle of the HWP up to 45°, the QWP angle at which the $g^{(2)}$ coefficient reaches its maximum is shifted towards larger angles. Also, the maximum and minimum $g^{(2)}$ values both decrease with larger HWP angles and exhibit values of 1.7 and 1, respectively. Increasing the HWP rotation angle beyond 45° an asymmetry of the $g^{(2)}$ values as a function of the QWP rotation angle becomes apparent. At an HWP angle of 45° the maximum $g^{(2)}$ values are located at a QWP angle of 45° and 135°, respectively, but they possess values of 1.7 and 1.4 each. The simulations of the communication keypad, as performed in the appendix, are depicted in Fig. 5, with red areas indicating a $g^{(2)}(\tau = 0)$ value of 2 and blue areas denoting a $g^{(2)}(\tau = 0)$ value of 1. Furthermore, the simulations clearly show that this asymmetry is caused by a retardation deviation of the HWP conditioned by the broad spectrum of the EDFA and the wavelength-dependent retardation of the nonideal HWP. There is a remarkable agreement between the simulations

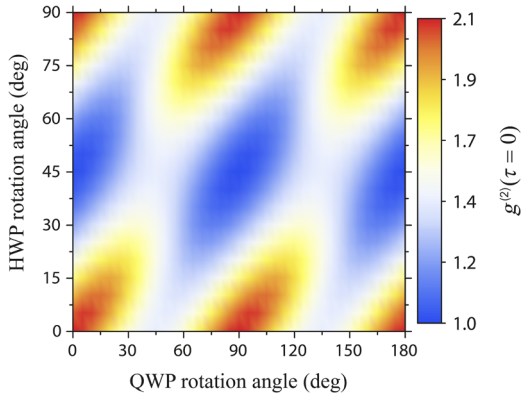

FIG. 5. Simulated communication keypad. Simulated map of $g^{(2)}(\tau = 0)$ values as a function of the HWP and QWP rotation angles for the case of a HWP with a nonideal retardation value of 0.55, calculated according to Eq. (A17). See Fig. 4 for comparison with the experimental data.

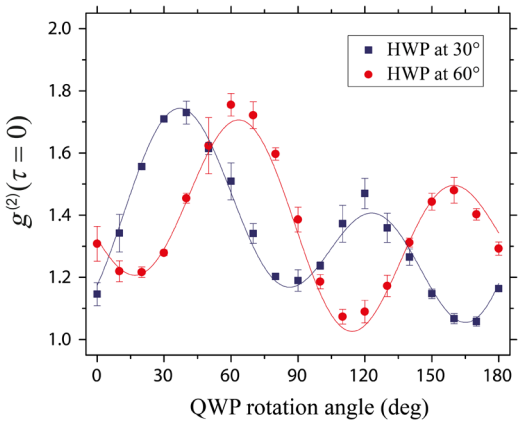

FIG. 6. Polarization correlations for QWP and HWP. $g^{(2)}(\tau = 0)$ values for two distinct rotation angles of the HWP (blue squares for an HWP angle of 30° and red circles for an HWP angle of 60°) as chosen by Alice plotted as a function of the rotation angle of Bob's QWP. The continuous lines are fitted to the data points using Eq. (A17) with a phase retardation of 0.55 for the HWP.

expressed by Eq. (A17) as depicted in Fig. 5 and the experimental data depicted in Fig. 4. This means that one can determine the HWP angle by measuring the $g^{(2)}(\tau = 0)$ values for well-selected QWP rotation angles. This is the reason why we call Figs. 4 and 5 the communication keypad.

These results thus allow an encoding and decoding of information and serve as the keypad for the GPC scheme. In the classical Stokes parameter analysis these values are hidden, as the polarization state of the unpolarized light does not change after passing the QWP and HWP. Therefore, these hidden angles can only be revealed by a measurement of the second-order correlation coefficient of the unpolarized light, which requires the original reference arm. Keeping the reference arm and the actual value of the QWP rotation angle securely in the hands of one party (Bob) and letting the other party (Alice) modify the IPS using an HWP, only Bob can reveal the HWP angle selected by Alice. This idea is exploited in the following to encode a message that is sent from Alice to Bob and is also an important point in the security issue discussion of Sec. IV.

C. Proof-of-principle message transfer

We make use of the fact that Bob can easily distinguish between the HWP rotation angles of 30° and 60°, even though after Alice's LP_O no change in intensity and polarization state can be observed. The communication scheme determining key relation is best illustrated by concentrating only on the two line plots extracted from the keypad results (Fig. 4), which are depicted in Fig. 6.

Figure 6 shows a line plot of the $g^{(2)}$ values as a function of the QWP rotation angle for two HWP rotation angles of 30° and 60° as measured by Bob. Here, the $g^{(2)}$ values show a modulation between 1.1 and 1.8, and in addition the two curves are shifted by approximately 30° for the two different HWP angles. Therefore, with the knowledge of the QWP rotation angle it is possible to distinguish between the two HWP angles (cf. the dashed lines in Fig. 4). For example, at a QWP angle of 120° the $g^{(2)}$ value amounts to 1.5 for a 30° rotation of the HWP, while it amounts to 1.1 for a 60° rotation. A differentiation of two bits is feasible at all QWP rotation angles, except at the angles at which the $g^{(2)}$ curves intersect each other as, for example, at 50°. Therefore, this clear separation allows an identification of a bit value of "1" associated with an HWP angle of 60° and a bit value of "0" with an angle of 30°. The results of Figs. 4 and 6 clearly show that even for nonideal wave plates and a range of values of $g^{(2)}$ between 1 to 2, there are always regimes for appropriate QWP and HWP angles, which result in clear and unambiguously identifiable values for "0" and "1" such that even considering the statistical error bars one could state in analogy to statistical communication language that there is "a clearly recognizable open eye." Alice now wants to send a message to Bob, which spells semiconductor optics (SCO) and is encoded in Baudot code [49]. This code allows us to transmit three letters by a total of 15 bits. In order to transfer the message, the following sequence is repeated until all bits are transmitted:

(a) Bob chooses a random QWP rotation angle;
(b) Alice adjusts the HWP to 30° (0 bit) or 60° (1 bit);
(c) Bob measures the $g^{(2)}$ coefficient and from this and the position of the QWP rotation angle, only known to him, he determines the HWP angle, respectively, the bit value using the full message key pad of Fig. 4 or the condensed one of Fig. 6.

TABLE I. Experimental results for the message transfer between Alice and Bob exemplarily showing the polarization encoding and decoding of the message "SCO."

QWP angle chosen by Bob (deg)	20	60	30	110	30	160	20	30	70	60	40	120	20	70	30
HWP angle chosen by Alice (deg)	60	30	30	30	60	30	60	60	30	60	30	30	60	60	60
$g^{(2)}(\tau = 0)$ value (± 0.05) measured by Bob	1.19	1.39	1.65	1.19	1.26	1.07	1.24	1.21	1.38	1.91	1.81	1.50	1.28	1.91	1.33
HWP angle read out by Bob (deg)	60	30	30	30	60	30	60	60	30	60	30	30	60	60	60
Corresponding bit sequence deduced by Bob (using Fig. 4)	1	0	0	0	1	0	1	1	0	1	0	0	1	1	1
Character (Baudot-Code)			**S**					**C**					**O**		

The result of the message transfer is summarized in Table I. The first row indicates the QWP rotation angle chosen by Bob and the second row shows Alice's chosen HWP angle. The measured $g^{(2)}$ values, together with an exemplaric error, are shown in the third row of the table, from which Bob determines the HWP angle (fourth row). These HWP angles are translated into bit values (fifth row) and finally 5 bits are used to decode a letter. As can be seen from the last row of Table I the message is correctly and securely received by Bob, which demonstrates the functionality of this proof-of-principle encoded message transfer.

IV. DISCUSSION

A. Real-life application

Currently, the bit transfer still takes approximately 4.5 min in total. In our proof-of-principle demonstration, we set the quarter-wave and half-wave plates' rotation angles manually or with motorized rotators. Clearly, this can also be realized by state-of-the-art polarization modulators with typical 100-MHz speed. This perspective holds in particular due to the fact our concept can be realized free space or fiber based at the telecom-relevant wavelength of 1.5 μm having access to all the currently used high-speed optoelectronic components. The actual real bottle neck on the level of this proof-of-principle demonstration is the speed of the interferogram acquisition thus limiting the bit rate. The $g^{(2)}$ extraction is performed with an interferometer and a TPA PMT required by the broadband spectrum ultra-fast correlation measurement. Modern high-speed interferometer mirror movers or displacers (e.g., "RockSolid" by Bruker) in Fourier-transform interferometers or loudspeaker-based interferometric correlators yield a much higher speed with appropriate sensitivity to accurately determine the interferometric autocorrelation function. In this spirit, one could also consider applying a spectral-filtering concept while keeping the polarization correlations but reducing the spectral width of the light such that the requirement $T_{\text{measure}} < 1/(\text{spectral width})$ is fulfilled with slower, nowadays available detectors. Fast single-photon counting avalanche photodiodes with subsequently following sophisticated signal analysis results in a quasi-real-time $g^{(2)}$ depiction. Recent studies [50] suggest a technique monitoring the temporal evolution of the $g^{(2)}$ values employing an ultra-fast phase-randomized homodyne detection setup. This eventually allows for a real-time "$g^{(2)}$ meter."

B. Security considerations

The elements of trust in secure communication systems are common to classical and quantum implementations of key distribution where in principle quantum key distribution can be made secure even though some threats to security remain that have been highlighted recently [51]. We emphasize that here we demonstrate an encoding principle that is currently not competing with well-established crypto systems but stands for an encoding principle based on camouflaging directly on the physical layer. We briefly discuss two obvious attack vectors used by an eavesdropper (Eve) for the setup we present here. For illustrative purposes, we assume our entire setup to be fiber based. The first attack is realized using an intensity measurement to obtain information about the HWP rotation angle by accessing the channel running from Alice to Bob. This attack is easily carried out using a clip-on fiber coupler to extract light from the fiber cladding by bending the fiber. However, incorporating an additional depolarizing element after Alice's LP_O renders this attack useless, since no information could be gained from the intensity measurement [38]. The second, more costly and sophisticated attack involves a similar correlation measurement between the two "attack points" accessible to Eve, one located between the QWP and the HWP and one between the LP_O and the interferometer stage. In order to give a qualitative impression of the security against such an attack we depict in Fig. 7 the results of these correlation measurements. A comparison of the maps measured by Bob (Fig. 4) and Eve (inset in Fig. 7) reveals a completely different behavior of the $g^{(2)}$

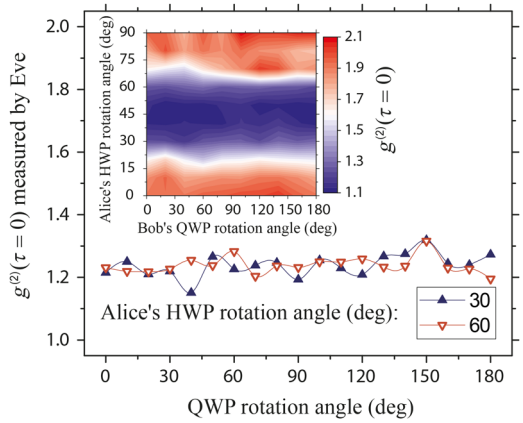

FIG. 7. Eve's correlation results. $g^{(2)}(\tau = 0)$ values for rotation angles of the HWP and QWP as measured by Eve while tapping the communication between Alice and Bob. Inset: entire map of all HWP rotation angles and all QWP rotation angles.

values with respect to the QWP and HWP rotation angles. The $g^{(2)}$ value measured by Bob depends on the rotation of the QWP, while this is constant for Eve. The inset and the condensed graphs clearly show that Eve has no means of differentiating between the chosen HWP angles of 30° and 60° and thus no means of extracting the message. In order to realize such an attack, Eve also has to scan for the interferometric center by measuring the length of the fiber on Alice's side and be able to physically establish a permanent connection between the two points of attack. Apart from being cost intensive for the attacker, this attack vector is also prone to being detected by Bob, due to the sensitivity of this interferometric setup. In both attack scenarios, the interferometric center is shifted and the polarization axis in the object channel is changed, immediately announcing the presence of an eavesdropper. Therefore, the sensitivity of this interferometric setup provides a built-in means of intrusion detection, which is absent in most data-transfer schemes apart from quantum cryptography.

V. SUMMARY AND CONCLUSIONS

A ghost polarization communication (GPC) scheme between two parties (Alice and Bob) is developed by exploiting the ultra-fast polarization dynamics of unpolarized thermal light and its photon correlation properties. By measuring the second-order correlation coefficient of unpolarized ASE light emitted by an EDFA utilizing a TPA PMT we reveal the IPS change after passing $\lambda/2$ and $\lambda/4$ wave plates in a Hanbury-Brown and Twiss like interferometer consisting of a reference and an object arm. While the IPS of the reference beam remained unchanged and enabled the message recovery, the IPS in the object arm is modified by a QWP and sent to Alice, who encodes her message by a further modification of the IPS using an HWP. Using this simple and robust scheme, we are able to encode and transfer a message between the two parties using standard off-the-shelf optical components, where the scheme can be realized both as a free-space or entirely fiber-based setup. The communication scheme we present here is the first application of ghost polarimetry, supported by a conclusive theoretical framework, which is presented in this paper. The $g^{(2)}(\tau = 0)$ measurement in ghost polarimetry can be regarded as the analog to a classical intensity measurement used in Stokes parameter analysis [52], thus also giving a fresh insight into polarization even more than 175 years after Stokes [40]. We are convinced that GPC opens completely new avenues of ghost modalities, as, e.g., enabling the combination of all so far realized ghost modalities such as ghost imaging, ghost spectroscopy, and ghost polarimetry. Finally, all hitherto realized ghost modalities are in principle possible without "ghost," e.g., "imaging" or "spectroscopy," and "ghost" only promotes a qualitative advantages over "nonghost." In this spirit, GPC is unique and represents a substantial breakthrough because GPC is solely possible due the recovery of the camouflaged polarization by correlations.

ACKNOWLEDGMENTS

The authors thank P. Janassek and S. Blumenstein for their support with the TPA PMT and fruitful and stimulating discussions. We acknowledge support by A. Herdt in completing the manuscript and in discussions. We thank Professor A.T. Friberg and Professor G. Genty for discussions about GI modalities. This work is supported by Deutsche Forschungsgemeinschaft (DFG) (project EL 105-21) and by Deutscher Akademischer Austauschdienst (DAAD) (project Breakthroughs in Ghost Imaging).

APPENDIX A: THEORY AND SIMULATIONS FOR THE POLARIZATION CORRELATIONS

To account for the observations in the change of the second-order correlation coefficient of the unpolarized light after interacting with the polarization optics, we develop a model where the instantaneous polarization state is represented by a temporally varying, single four-valued Stokes vector $\vec{S}_{\text{in}}(r, \theta, \phi)$ with the polarization components S_1, S_2, and S_3 written in spherical coordinates [53]:

$$\vec{S}_{\text{in}}(t) = \vec{S}_{\text{in}}(r, \theta, \phi) = \begin{pmatrix} S_0 \\ S_1 \\ S_2 \\ S_3 \end{pmatrix} = \begin{pmatrix} r \\ r\cos(\theta) \\ r\sin(\theta)\cos(\phi) \\ r\sin(\theta)\sin(\phi) \end{pmatrix}, \tag{A1}$$

where the radius $r(t)$, azimuthal angle $\phi(t)$, and the polar angle $\theta(t)$ are time dependent. In the following, for the sake of brevity we omit the time dependence t. The Stokes vectors $\vec{S}$ for both the reference beam and the object beam

after having traversed the polarization optics can be calculated using the input Stokes vector $\vec{S}_{\text{in}}$ behind the beam splitter using the following Mueller matrix formalism:

$$\vec{S}_{\text{ref}} = M_{\text{ref}}\vec{S}_{\text{in}} = M_{\text{LP}_R}\vec{S}_{\text{in}}, \tag{A2}$$

$$\vec{S}_{\text{obj}} = M_{\text{obj}}\vec{S}_{\text{in}}. \tag{A3}$$

Here, M_{LP_R} is the Mueller matrix for a linear polarizer. The matrix for M_{obj} is a product of Mueller matrices, which depends on the constellation of polarization optics placed in the object beam and is written as follows for the case depicted in Fig. 1:

$$\begin{aligned} M_{\text{obj}} &= \begin{pmatrix} a_{11} & \dots & a_{14} \\ \vdots & & \vdots \\ a_{41} & \dots & a_{44} \end{pmatrix} \\ &= M_{\text{LP}_O} M_{\text{HWP}}(\beta) M_{\text{QWP}}(\alpha), \end{aligned} \tag{A4}$$

where α is the QWP rotation angle and β is the HWP rotation angle with respect to the polarization axis of the LP_O. The intensity of both the object beam and the reference beam that impinges on the PMT corresponds to the first element S_0 of each Stokes vector: $S_{\text{obj},0}$ and $S_{\text{ref},0}$. In order to calculate the $g^{(2)}(\tau = 0)$ values, these first elements are used to formulate the following expression, according to the second-order correlation expression in a ghost imaging protocol [31,54], with both $S_{\text{ref},0}$ and $S_{\text{obj},0}$ containing dependencies on the wave-plate rotation angles α and β:

$$g^{(2)}(\tau = 0) = \frac{\langle S_{\text{ref},0} S_{\text{obj},0} \rangle}{\langle S_{\text{ref},0} \rangle \langle S_{\text{obj},0} \rangle}. \tag{A5}$$

In this expression, the brackets indicate a generalized ensemble average over time [42]. By inserting Eq. (A2) and (A3) into Eq. (A5), we obtain the following expression:

$$\begin{aligned} &g^{(2)}(\tau = 0) \\ &\quad = \frac{\langle (S_0 + S_1)(a_{11}S_0 + a_{12}S_1 + a_{13}S_2 + a_{14}S_3) \rangle}{\langle S_0 + S_1 \rangle \langle a_{11}S_0 + a_{12}S_1 + a_{13}S_2 + a_{14}S_3 \rangle}. \end{aligned} \tag{A6}$$

Further evaluation of this equation contains terms of the form $\langle S_i \rangle$ and $\langle S_i S_j \rangle$, which are the ensemble averages and moments of the time-dependent Stokes parameters $S_i(t)$, respectively. These terms have already been evaluated for unpolarized light of a Gaussian field [55]. Within this context, the relevant ensemble averages and the moments that are found by multiplying the terms in Eq. (A6) are listed below:

$$\langle S_0 \rangle = \langle I \rangle, \tag{A7}$$

$$\langle S_1 \rangle = \langle S_2 \rangle = \langle S_3 \rangle = 0, \tag{A8}$$

$$\langle S_0 S_0 \rangle = \left(\frac{\langle I \rangle}{2} \right)^2 \cdot 3 \cdot 2 = 1.5 \langle I \rangle^2, \tag{A9}$$

$$\langle S_1 S_1 \rangle = \left(\frac{\langle I \rangle}{2} \right)^2 \cdot \frac{6}{3} = 0.5 \langle I \rangle^2. \tag{A10}$$

Inserting these results for the moments into Eq. (A6) yields the following expression for the $g^{(2)}(\tau = 0)$ values in our ghost polarimetry setup:

$$g^{(2)}(\tau = 0) = \frac{1.5 a_{11} \langle I \rangle^2 + 0.5 a_{12} \langle I \rangle^2}{\langle I \rangle a_{11} \langle I \rangle} = 1.5 + \frac{a_{12}}{2a_{11}}. \tag{A11}$$

Here, the factors a_{11} and a_{12} are the first two elements of the first row of M_{obj} in Eq. (A4) obtained from the matrix multiplications according to Eq. (A3).

To substantiate the validity of our model, we apply it to the measured $g^{(2)}(\tau = 0)$ values for the various constellations of polarization optics presented in the results of this paper. In the following equations, all polarization optics are represented by their corresponding 4×4 Mueller matrix [53]. For the experiment with only the LP_R in the reference arm and the LP_O in the object arm, the matrix multiplications take the following form:

$$\begin{aligned} \vec{S}_{\text{ref}} &= M_{\text{LP}_R}(\vartheta)\vec{S}_{\text{in}} = M_{\text{ref}}\vec{S}_{\text{in}}, \\ \vec{S}_{\text{obj}} &= M_{\text{LP}_O}\vec{S}_{\text{in}} = M_{\text{obj}}\vec{S}_{\text{in}}, \end{aligned} \tag{A12}$$

where ϑ is the rotation angle of the polarizer LP_R. After having evaluated the matrix multiplications, we derive the fit function for the $g^{(2)}(\tau = 0)$ values as expressed by Eq. (1). For the case of the additional HWP in front of the LP_O, the matrix multiplications have this form:

$$\begin{aligned} \vec{S}_{\text{ref}} &= M_{\text{LP}_R}(\vartheta)\vec{S}_{\text{in}} = M_{\text{ref}}\vec{S}_{\text{in}}, \\ \vec{S}_{\text{obj}} &= M_{\text{LP}_O} M_{\text{HWP}}(\beta)\vec{S}_{\text{in}} = M_{\text{obj}}\vec{S}_{\text{in}}, \end{aligned} \tag{A13}$$

where ϑ is the rotation angle of the polarizer LP_R and β is the HWP rotation angle. The resulting fit function for the $g^{(2)}(\tau = 0)$ values in this case is expressed by Eq. (3). In analogy, for the case with the QWP in the object arm, the Stokes vectors in both arms are calculated as

$$\begin{aligned} \vec{S}_{\text{ref}} &= M_{\text{LP}_R}(\vartheta)\vec{S}_{\text{in}} = M_{\text{ref}}\vec{S}_{\text{in}}, \\ \vec{S}_{\text{obj}} &= M_{\text{LP}_O} M_{\text{QWP}}(\alpha)\vec{S}_{\text{in}} = M_{\text{obj}}\vec{S}_{\text{in}}, \end{aligned} \tag{A14}$$

where ϑ is the rotation angle of the polarizer LP_R and α is the QWP rotation angle. This yields the expression for the fit function for the $g^{(2)}(\tau = 0)$ values in Eq. (4). For the final setup, which contains two polarizers and two wave

plates in the appropriate positions of reference arm and object arm (see Fig. 1), the Stokes vectors are

$$\begin{aligned}\vec{S}_{\mathrm{ref}} &= M_{\mathrm{LP}_R}\vec{S}_{\mathrm{in}} = M_{\mathrm{ref}}\vec{S}_{\mathrm{in}},\\ \vec{S}_{\mathrm{obj}} &= M_{\mathrm{LP}_O}M_{\mathrm{HWP}}(\beta)M_{\mathrm{QWP}}(\alpha)\vec{S}_{\mathrm{in}} = M_{\mathrm{obj}}\vec{S}_{\mathrm{in}},\end{aligned} \tag{A15}$$

where α is the QWP rotation angle and β the HWP rotation angle with respect to the polarization axis of the LP_O. From this, we calculate the following fit function for the $g^{(2)}(\tau = 0)$ values:

$$\begin{aligned}g^{(2)}(\tau = 0, \alpha, \beta) = 1.5 &+ 0.25\cos[4(\alpha - \beta)]\\ &+ 0.25\cos(4\beta).\end{aligned} \tag{A16}$$

We now perform a comparison between the $g^{(2)}(\tau = 0)$ values obtained from the developed model and the actually measured values of the second-order correlation coefficient for the setup with both the QWP and HWP. In this setup, we keep both linear polarizers fixed in parallel and adjust the HWP to 30° and to to 60°, respectively and measure $g^{(2)}(\tau = 0)$ values as a function of the rotation angle of the QWP. The results of these measurements are shown in Fig. 6 (30°, blue squares; 60°, red dots) and are essentially the two line plots extracted from the keypad of Fig. 4. First of all it can be seen, that the measured $g^{(2)}(\tau = 0)$ exhibit local minima and maxima for the measured rotation angles of the QWP in comparison to the curves in Fig. 3. The measured values are located between 1.1 and 1.8 and besides this minimum and maximum values a local minimum of 1.2 and a local maximum of 1.5 is observed. The shape for both curves is similar, but the minimum and maximum values are shifted by 32° towards higher QWP rotation angles. A trial to perform a curve fitting to the measured data using the developed model [Eq. (A16)] is unable to accurately reproduce the asymmetry of the local maxima. Therefore, the curve fitting is performed using a more comprehensive expression for the $g^{(2)}(\tau = 0)$ values to account for the influence of the nonideal phase retardation of the half-wave plate and the spectrally broadband source used in our setup:

$$\begin{aligned}&g^{(2)}(\tau = 0, \alpha, \beta, \phi)\\ &\quad= 1.5 + \cos^2(2\alpha)(0.5\cos^2(2\beta)\\ &\qquad+ 0.5\cos(2\pi\phi)\sin^2(2\beta))\\ &\qquad+ [0.125 - 0.125\cos(2\pi\phi)]\sin(4\alpha)\sin(4\beta)\\ &\qquad- 0.5\sin(2\alpha)\sin(2\beta)\sin(2\pi\phi).\end{aligned} \tag{A17}$$

Here α and β are the rotation angles of the QWP and HWP, respectively and ϕ is the retardation of the HWP. It should be noted, that by setting $\phi = 0.5$, we obtain Eq. (A16). Only by introducing a retardation, which deviates from the value 0.5 of an ideal HWP, the measurements can be reproduced. This nonideal retardation causes the additional local minimum and maximum values and is a result of the wavelength-dependent retardation of the utilized HWP and the broad spectrum [56] of the EDFA. From the curve fitting a value of 0.55 is obtained for the retardation of the HWP. The results of this curve fitting to the measured data using the developed model are shown as solid lines in the corresponding color in Fig. 6. Comparing the curve fitting result with the corresponding measured data in Fig. 6 a very good agreement is found, which is also reflected in the high R-square values of 0.97 and 0.94 of our fits for the case of a HWP rotation angle of 30° and 60°, respectively.

While the intensity measured after the linear polarizer LP_O is constant, regardless of the rotation angles of the QWP and HWP, the measured $g^{(2)}(\tau = 0)$ values depend on these rotation angles. The minimum and maximum values do not only shift as demonstrated by the measurements and simulations in this section, also the corresponding difference in minimum and maximum change with respect to the HWP angle. This leads to a situation in which a pair of HWP and QWP angles clearly determine the $g^{(2)}(\tau = 0)$ value, being the basis for the complete experimentally determined keypad depicted in Fig. 4 accompanied by the simulated key pad according to Eq. (A17) and depicted in Fig. 5.

[1] Steven Aftergood, Cybersecurity: The cold war online, Nature **547**, 30 (2017).

[2] R. L. Rivest, A. Shamir, and L. Adleman, A method for obtaining digital signatures and public-key cryptosystems, Commun. ACM **21**, 120 (1978).

[3] D. Boneh, Twenty years of attacks on the rsa cryptosystem, Not. Am. Math. Soc. **46**, 203 (1999).

[4] Peter W. Shor, Polynomial-time algorithms for prime factorization and discrete logarithms on a quantum computer, SIAM J. Comput. **26**, 1484 (1997).

[5] Gilles Brassard, Norbert Lütkenhaus, Tal Mor, and Barry C. Sanders, in *Advances in Cryptology – EUROCRYPT 2000*, edited by Bart Preneel (Springer, Berlin Heidelberg, 2000), p. 289.

[6] Gabriel Popkin, Quest for qubits, Science **354**, 1090 (2016).

[7] D. J. Bernstein and T. Lange, Post-quantum cryptography, Nature **549**, 188 (2017).

[8] Charles H. Bennett and Gilles Brassard, Quantum cryptography: Public key distribution and coin tossing, Theor. Comput. Sci. **560**, 7 (2014).

[9] Mario Krenn, Mehul Malik, Thomas Scheidl, Rupert Ursin, and Anton Zeilinger, in *Optics in Our Time* (Springer International Publishing, Cham, 2016), p. 455.

[10] W. K. Wootters and W. H. Zurek, A single quantum cannot be cloned, Nature **299**, 802 (1982).

[11] Artur K. Ekert, Quantum Cryptography Based on Bell's Theorem, Phys. Rev. Lett. **67**, 661 (1991).

[12] Th. Jennewein, Ch. Simon, G. Weihs, H. Weinfurter, and A. Zeilinger, Quantum Cryptography with Entangled Photons, Phys. Rev. Lett. **84**, 4729 (2000).

[13] R. Ursin, F. Tiefenbacher, T. Schmitt-Manderbach, H. Weier, T. Scheidl, M. Lindenthal, B. Blauensteiner, T. Jennewein, J. Perdigues, P. Trojek, B. Ömer, M. Fürst, M. Meyenburg, J. Rarity, Z. Sodnik, C. Barbieri, H. Weinfurter, and A. Zeilinger, Entanglement-based quantum communication over 144 km, Nat. Phys. **3**, 481 (2007).

[14] Alicia Sit, Frédéric Bouchard, Robert Fickler, Jérémie Gagnon-Bischoff, Hugo Larocque, Khabat Heshami, Dominique Elser, Christian Peuntinger, Kevin Günthner, Bettina Heim, Christoph Marquardt, Gerd Leuchs, Robert W. Boyd, and Ebrahim Karimi, High-dimensional intracity quantum cryptography with structured photons, Optica **4**, 1006 (2017).

[15] Juan Yin *et al.*, Satellite-based entanglement distribution over 1200 kilometers, Science **356**, 1140 (2017).

[16] B. Korzh, C. C. W. Lim, R. Houlmann, N. Gisin, M. J. Li, D. Nolan, B. Sanguinetti, R. Thew, and H. Zbinden, Provably secure and practical quantum key distribution over 307 km of optical fibre, Nat. Photonics **9**, 163 (2015).

[17] Laurent Larger and Jean-Pierre Goedgebuer, Encryption using chaotic dynamics for optical telecommunications, C. R. Phys. **5**, 609 (2004).

[18] Tilmann Heil, Josep Mulet, Ingo Fischer, Claudio R. Mirasso, Michael Peil, P. Colet, and W. Elsäßer, On/off phase shift keying for chaos-encrypted communication using external-cavity semiconductor lasers, IEEE J. Quantum Electron. **38**, 1162 (2002).

[19] Apostolos Argyris, Evangelos Grivas, Adonis Bogris, and Dimitris Syvridis, Transmission effects in wavelength division multiplexed chaotic optical communication systems, J. Lightwave Technol. **28**, 3107 (2010).

[20] Raúl Vicente, Claudio R. Mirasso, and Ingo Fischer, Simultaneous bidirectional message transmission in a chaos-based communication scheme, Opt. Lett. **32**, 403 (2007).

[21] Andrew S. Tanenbaum and David J. Wetherall, *Computer Networks* (Pearson, Boston, 2010).

[22] A. Argyris, D. Syvridis, L. Larger, V. Annovazzi-Lodi, P. Colet, I. Fischer, J. Garcia-Ojalvo, C. R. Mirasso, L. Pesquera, and A. Shore, Chaos-based communications at high bit rates using commercial fibre-optic links, Nature **438**, 343 (2005).

[23] C. R. Mirasso, I. Fischer, M. Peil, and L. Larger, Optoelectronic devices for optical chaos communications, Proc. SPIE **5248**, 24 (2003).

[24] C. R. Mirasso, Chaotic optical communications, IEEE LEOS Newsl. **19**, 12 (2005).

[25] Mehrdad Tanha, Reza Kheradmand, and Sohrab Ahmadi-Kandjani, Gray-scale and color optical encryption based on computational ghost imaging, Appl. Phys. Lett. **101**, 101108 (2012).

[26] Wen Chen and Xudong Chen, Ghost imaging using labyrinth-like phase modulation patterns for high-efficiency and high-security optical encryption, EPL (Europhysics Lett.) **109**, 14001 (2015).

[27] T. B. Pittman, Y. H. Shih, D. V. Strekalov, and A. V. Sergienko, Optical imaging by means of two-photon quantum entanglement, Phys. Rev. A **52**, R3429 (1995).

[28] Ryan S. Bennink, Sean J. Bentley, and Robert W. Boyd, "Two-Photon" Coincidence Imaging with a Classical Source, Phys. Rev. Lett. **89**, 113601 (2002).

[29] F. Ferri, D. Magatti, A. Gatti, M. Bache, E. Brambilla, and L. A. Lugiato, High-Resolution Ghost Image and Ghost Diffraction Experiments with Thermal Light, Phys. Rev. Lett. **94**, 183602 (2005).

[30] Baris I. Erkmen and Jeffrey H. Shapiro, Unified theory of ghost imaging with gaussian-state light, Phys. Rev. A **77**, 043809 (2008).

[31] S. Hartmann and W. Elsäßer, A novel semiconductor-based, fully incoherent amplified spontaneous emission light source for ghost imaging, Sci. Rep. **7**, 41866 (2017).

[32] S. Karmakar, R. Meyers, and Y. Shih, Ghost imaging experiment with sunlight compared to laboratory experiment with thermal light, Proc. SPIE Quantum Commun. Quantum Imaging X **8518**, 851805 (2012).

[33] Patrick Janassek, Sébastien Blumenstein, and Wolfgang Elsäßer, Ghost Spectroscopy with Classical Thermal Light Emitted by a Superluminescent Diode, Phys. Rev. Appl. **9**, 021001 (2018).

[34] Patrick Janassek, Andreas Herdt, Sébastien Blumenstein, and Wolfgang Elsäßer, Ghost spectroscopy with classical correlated amplified spontaneous emission photons emitted by an erbium-doped fiber amplifier, Appl. Sci. **8**, 1896 (2018).

[35] Patrick Janassek, Sébastien Blumenstein, and Wolfgang Elsäßer, Ghost spectroscopy, Opt. Photonics News **29**, 41 (2018).

[36] P. Ryczkowski, M. Barbier, A. T. Friberg, J. M. Dudley, and G. Genty, Ghost imaging in the time domain, Nat. Photonics **10**, 167 (2016).

[37] Fabrice Devaux, Paul-Antoine Moreau, Severine Denis, and Eric Lantz, Computational temporal ghost imaging, Optica **3**, 698 (2016).

[38] Patrick Janassek, Sébastien Blumenstein, and Wolfgang Elsäßer, Recovering a hidden polarization by ghost polarimetry, Opt. Lett. **43**, 883 (2018).

[39] T. Heil, J. Mulet, I. Fischer, C. R. Mirasso, M. Peil, P. Colet, and W. Elsäßer, On/off phase shift keying for chaos-encrypted communication using external-cavity semiconductor lasers, IEEE J. Quantum Elect. **38**, 1162 (2002).

[40] G. G. Stokes, On the composition and resolution of streams of polarized light from different sources, Trans. Cambridge Philos. Soc. **9**, 399 (1852), Reprinted in Mathematical and Physical Papers by Cambridge University Press (2009).

[41] We recall that within the framework of the classical Stokes formalism, the polarization state of light is regarded on time scales several magnitudes larger than the period of the oscillating electromagnetic field [52].

[42] Tero Setälä, Andriy Shevchenko, Matti Kaivola, and Ari T. Friberg, Polarization time and length for random optical beams, Phys. Rev. A **78**, 033817 (2008).

[43] Gregory D. VanWiggeren and Rajarshi Roy, Communication with Dynamically Fluctuating States of Light Polarization, Phys. Rev. Lett. **88**, 097903 (2002).

[44] Andriy Shevchenko, Matthieu Roussey, Ari T. Friberg, and Tero Setälä, Polarization time of unpolarized light, Optica **4**, 64 (2017).

[45] Due to the similarity of our setup with the ghost polarimetry [38] setup, we keep the nomenclature of "reference arm" and "object arm".
[46] F. Boitier, A. Godard, E. Rosencher, and C. Fabre, Measuring photon bunching at ultrashort timescale by two-photon absorption in semiconductors, Nat. Phys. **5**, 267 (2009).
[47] Rodney Loudon, *The Quantum Theory of Light* (Oxford University Press, Oxford, 2000).
[48] W. A. Shurcliff and S. S. Stanley, *Polarized Light* (D. Van Nostrand Company, Princeton, New Jersey, 1964).
[49] F. G. Heath, Origins of the binary code, Sci. Am. **227**, 76 (1972).
[50] Carolin Lüders, Johannes Thewes, and Marc Assmann, Real time g(2) monitoring with 100 khz sampling rate, Opt. Express **26**, 24854 (2018).
[51] V. Scarani and Ch. Kurtsiefer, The black paper of quantum cryptography: Real implementation problems, Theor. Comput. Sci. **560**, 27 (2014).
[52] A. Molitor, T. Mohr, S. Hartmann, and W. Elsäßer, Investigations on spectro-temporally resolved stokes polarization parameters of transverse multi-mode vertical-cavity surface-emitting lasers, IEEE J. Quantum Electron. **52**, 1 (2016).
[53] E. Collet, *Polarized Light: Fundamentals and Applications* (Marcel Dekker, New York, 1993).
[54] Roy J. Glauber, The quantum theory of optical coherence, Phys. Rev. **130**, 2529 (1963).
[55] Danny Eliyahu, Statistics of stokes variables for correlated gaussian fields, Phys. Rev. E **50**, 2381 (1994).
[56] The FWHM is measured to be 4.4 nm at an optical output power of 4.6 mW.